

First Principles Studies of Fe-Containing Aluminosilicate and Aluminogermanate Nanotubes

Fernando Alvarez-Ramírez

*Instituto Mexicano del Petróleo, Programa de Ingeniería Molecular, Eje Central
Lázaro Cárdenas 152, 07730, México, Distrito Federal, México.*

Received June 09, 2009

Abstract: A theoretical study of the electronic effects of the inclusion of iron on aluminosilicates and aluminogermanates nanotubes with imogolite-like structure was carried out by unrestricted all-electron density functional theory calculations of periodic boundary models. The iron ion was incorporated to the imogolitic models by an isomorphic substitution of Al by Fe and by the adsorption of the Fe ion in the inner and outer nanotube structure in the octahedral hydrated configuration. Additionally, the effects of the Fe concentration in the interval $0.05 \leq x \leq 0.1$ were analyzed. We observe a drastic reduction of the bandgap value from 4.6 to 2.6 eV and from 4.2 to 1.0 eV for the silicon and germanium respectively. Finally, in all the models there is a shift of the Fermi energy toward the gap region as a result of the inclusion of iron electronic states in the bandgap region.

Introduction

Imogolite denotes mineral nanotubes compounds with chemical formula $(\text{OH})_3\text{Al}_2\text{O}_3\text{SiOH}$, which manifests the atomic layer arrangement going from the exterior to the interior of the nanotube wall. Mineral imogolite is mostly found in soils derived from volcanic ash and in weathered pumices and spodosols.^{1,2} Imogolite-like aluminosilicates (Si-Imo) and aluminogermanates (Ge-Imo) have been synthesized by hydrothermal reactions at relatively low temperature of stirred diluted solutions of aluminum chloride [AlCl_3] as source of aluminum and tetraethylorthosilicate $\text{Si}(\text{OC}_2\text{H}_5)_4$ and tetraethylorthogermanate $\text{Ge}(\text{OC}_2\text{H}_5)_4$ as sources of silicon and germanium respectively.^{3–5} Recently renovated efforts have been carried out toward a more efficient qualitative and quantitative synthesis procedure of imogolite-like structures.^{6–8} Natural imogolites and its synthetic nanotube analog structures ($(\text{OH})_3\text{Al}_2\text{O}_3\text{SiOH}$, Si-Imo) and ($(\text{OH})_3\text{Al}_2\text{O}_3\text{GeOH}$, Ge-Imo) can be applied in the field of chemical sorption reactivity,⁹ membrane,¹⁰ humidity controlling,¹¹ catalysis support.^{12,13}

Despite the imogolite-like structures being proposed as good candidates for catalytic applications, because of properties such as large surface areas, which vary from $200 \text{ m}^2/\text{g}$ to above $700 \text{ m}^2/\text{g}$, depending on absorbate^{4,10} and the charge properties in the inner-outer walls, in most cases these

volclays exhibit little or no catalysis because of chemical stability. Therefore, the incorporation of different metallic elements on the imogolites surface (Cr, Mo, W, V, Fe, Ni, Co),¹⁴ (Cd, Cu, Pd),⁹ Ag,¹⁵ or active catalytic molecules¹⁶ is necessary to improve their catalytic activity. The imogolite-metal ion dimer can be synthesized by a direct impregnation on the imogolite surface of the metallic ions being the imogolite surface the support for the catalytic metal species.^{9,13,14,16} An alternative route for the incorporation of the metallic ions to the imogolite structure/surface is a direct addition of the metal ions in the gel-like precursors.^{13,17}

Natural imogolite is commonly found in association with short-range-order materials like allophane and ferrihydrite in many Andisols, where the iron is one of the most recurrent contaminants of imogolite and other soil clays.^{18–20} However, the phenomenon of the incorporation or segregation of Fe^{3+} ions from and toward the nanotube is not completely answered because the difficulties in the interpretation of the configuration and atomic environment of the iron ions in the soil-like materials. On the basis of electron spin resonance (ESR) spectroscopy McBride et al.¹⁷ suggested that little or no Fe^{3+} is incorporated to the imogolite structure, observing the tendency of the Al and the Fe to segregate into imogolite and ferrihydrite structures respectively. In their studies, McBride et al. observed the formation of imogolite fibres in preparations with Al/Fe ratios of larger than 9 and the

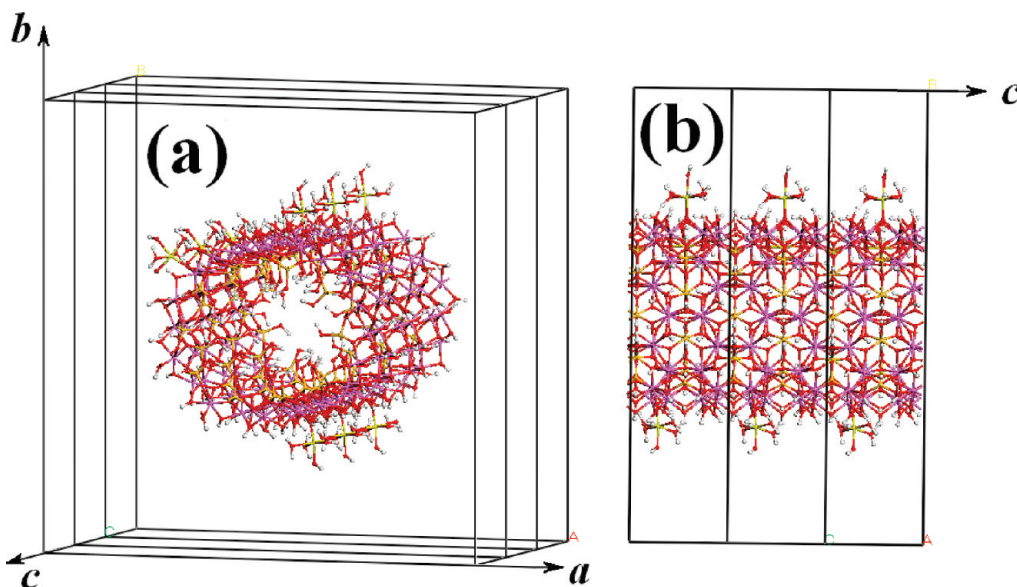


Figure 1. (a) Periodic boundary conditions used in the Fe-imogolite calculations. (b) Periodic conditions along the fiber axis, *c*

formation of ferrihydrite for Al/Fe ratio of 1 and 0.25, deducing that the tube formation is inhibited by Al/Fe ratios of one or less.

On the other hand, Ookawa et al.¹³ reported the synthesis of iron containing imogolites with atomic ratio between $x = \text{Fe}/(\text{Fe} + \text{Al}) = 0.05$ and 0.1 (Al/Fe = 9 and 19, respectively), where the iron ions are added to the fibres by two routes. In the first route the Fe^{3+} ions source, FeCl_3 , are incorporated directly to aqueous solutions of Na_4SiO_4 and $\text{AlCl}_3 \cdot 6\text{H}_2\text{O}$, denoting this route as (Imo-Fe). In the second route the Fe^{3+} ions are absorbed directly on the imogolite denoting this process as Imo/Fe. Based on UV-vis and XANES spectra, Ookawa et al. observed the octahedral configuration as the preferred disposition of the Fe^{3+} ions in both Imo-Fe and Imo/Fe routes. Additionally, based on k3-weighted EXAFS function and its Fourier transformation (FT), Ookawa et al. argues the formation of different Fe ion states between the routes Imo-Fe and Imo/Fe. However, the electronic effect of the substitution of Al^{3+} by the Fe^{3+} in the imogolite was not totally elucidated. The inclusion of ferric species like the ferric chloride hexahydrate ($\text{FeCl}_3 \cdot 6\text{H}_2\text{O}$) to the imogolite structure is not limited to the case of adsorption process in the imogolite, it is also being applied in the preparation of ppy-imogolite (polypyrrole (ppy)) hybrid materials where the iron acts as an oxidant in the mechanism of polymerization of (ppy).²¹

The aim of this work is to study from the point of view of first principles some of the electronic properties of the iron ion inclusion into and on the imogolite structure and its structural analogue germanate, $(\text{OH})_3\text{Al}_2\text{O}_3\text{GeOH}$, to help in the electronic interpretation of the experimental phenomenology of the incorporation or segregation of Fe^{3+} ions from and toward the imogolite nanotube.

Methodology

To simulate the pseudocrystalline one-dimensional structure of the Fe-imogolite-like fibers, a sequence of models with

periodic boundary conditions were built taking as structural imogolite the standard model reported by Wada et al.^{2,22} and Farmer et al.⁵ The skeleton of the iron containing imogolite-like structure is a model with ten gibbsite units, $N_u = 10$, considered as the most likely structure model of natural imogolite.²³ The dimensions of the rectangular simulation cells along the tubular axial direction (*c*, Figure 1) were chosen as 8.78 and 8.8 Å for the silicon and germanium containing structures respectively on the basis of previous calculations using the Γ point approximation.²⁴ The transversal cell lengths *a* and *b* were chosen to be 40 Å to inhibit the interaction of the imogolite images along these non axial directions because the periodic boundary conditions of the models, Figure 1. In our case the *c* cell length is slightly larger than the experimental X-ray diffraction value for aluminosilicate and the aluminagermanate imogolite-like structures, that is, 8.51 Å. This overestimation has been reported as a consequence of the semilocal density functional approximation in the case of aluminosilicates.^{25–28}

Experimental reports of McBride et al.¹⁷ show the fibrous structure are preserved only in the cases where the ratio $\text{Al}/\text{Fe} \leq 9$. Therefore; the iron containing in our models was restricted to values above this critical threshold. As regards to the iron ions localization, they were located in three different qualitative imogolite places. The first iron localization corresponds to the isomorphic substitution of Al^{3+} by Fe^{3+} ions in the imogolite atomic layer denoted as Al_5 in Figure 2a and b; this configuration plays the role of iron absorbed on the imogolite structure in a similar way to the Imo-Fe structure reported by Ookawa et al.¹³ This kind of configuration was in this work simulated by four models with isomorphic substitution of one to four Al^{3+} atoms by Fe^{3+} which corresponds to $x = (0.025, 0.05, 0.075, 0.1)$ with a general notation M-Imo-Fe, see Table 1 and Supporting Information.

The two remaining iron configurations corresponds to the case where the iron atom is adsorbed on the inner or the

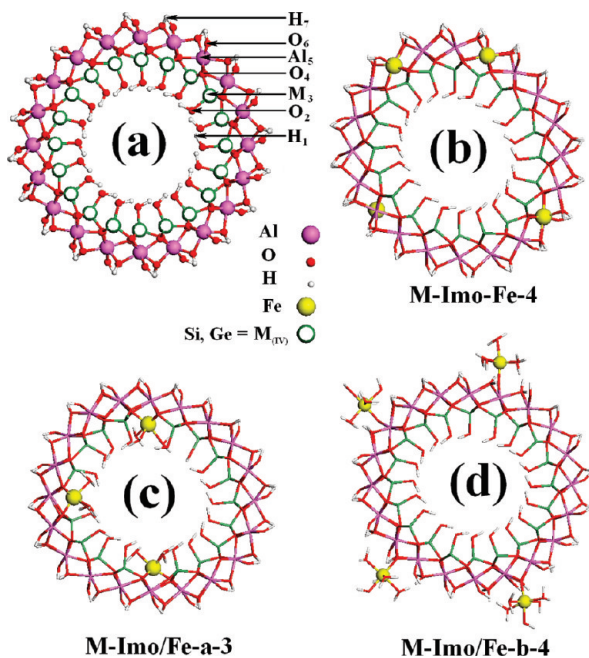


Figure 2. (a) Transversal section of the imogolite structure where is indicated the notation of the atomic layers in the structure. (b) Schematic representation of octahedral isomorphic substitution of Al^{3+} for Fe^{3+} . (c–d) Adsorption of octahedral Fe^{3+} ions on the inner and outer imogolite surface. In all the cases the M symbol denotes both Si or Ge containing structures.

Table 1. Notation Use in the Fe-Containing Aluminosilicate and Aluminogermanate Nanotubes Analyzed in This Work^a

compound	short name	x	Al/Fe	class
$\text{H}_{80}\text{O}_{140}\text{Al}_{39}\text{Fe}_1\text{M}_{20}$	M- <i>Imo</i> -Fe-1	0.025	39.0	subst
$\text{H}_{80}\text{O}_{140}\text{Al}_{38}\text{Fe}_2\text{M}_{20}$	M- <i>Imo</i> -Fe-2	0.050	10.0	subst
$\text{H}_{80}\text{O}_{140}\text{Al}_{37}\text{Fe}_3\text{M}_{20}$	M- <i>Imo</i> -Fe-3	0.075	12.3	subst
$\text{H}_{80}\text{O}_{140}\text{Al}_{36}\text{Fe}_4\text{M}_{20}$	M- <i>Imo</i> -Fe-4	0.100	9.0	subst
$\text{H}_{85}\text{O}_{142}\text{Al}_{40}\text{Fe}_1\text{M}_{19}$	M- <i>Imo</i> /Fe-a-1	0.024	40.0	inner/abs
$\text{H}_{90}\text{O}_{144}\text{Al}_{40}\text{Fe}_2\text{M}_{18}$	M- <i>Imo</i> /Fe-a-2	0.048	20.0	inner/abs
$\text{H}_{95}\text{O}_{146}\text{Al}_{40}\text{Fe}_3\text{M}_{17}$	M- <i>Imo</i> /Fe-a-3	0.070	13.3	inner/abs
$\text{H}_{100}\text{O}_{148}\text{Al}_{40}\text{Fe}_4\text{M}_{16}$	M- <i>Imo</i> /Fe-a-4	0.090	10.0	inner/abs
$\text{H}_{87}\text{O}_{145}\text{Al}_{40}\text{Fe}_1\text{M}_{20}$	M- <i>Imo</i> /Fe-b-1	0.024	40.0	outer/abs
$\text{H}_{94}\text{O}_{150}\text{Al}_{40}\text{Fe}_2\text{M}_{20}$	M- <i>Imo</i> /Fe-b-2	0.048	20.0	outer/abs
$\text{H}_{101}\text{O}_{155}\text{Al}_{40}\text{Fe}_3\text{M}_{20}$	M- <i>Imo</i> /Fe-b-3	0.070	13.3	outer/abs
$\text{H}_{108}\text{O}_{160}\text{Al}_{40}\text{Fe}_4\text{M}_{20}$	M- <i>Imo</i> /Fe-b-4	0.090	10.0	outer/abs

^a The M symbol denotes the Si or Ge aluminosilicate nanotube variation. On the other hand, the notation subst, inner/abs and outer/abs corresponds with the Fe^{3+} in the imogolite-like structure as is shown in Figure 2a and Figures S1 and S2 of the supporting information.

outer the imogolite surfaces producing surface defects in the standard imogolite model being this kind of configuration similar to the Ookawa's Imo/Fe arrangement.¹³ In the first Imo/Fe configuration denoted in general as M-*Imo*/Fe-a, see Table 1, the iron atom substitutes the element of the group IV (layer M_3 in Figure 2a) in the pore tubular region, being linked to three oxygen atoms of the O_4 layer, Figure 2a. Because the octahedral disposition is the preferred configuration of the Fe^{3+} ions a hydrated sphere of three water molecules were added to the iron ion to preserve both the octahedral iron configuration and the oxidation 3+, Figure 2c.

The second Imo/Fe configuration denoted in general as M-*Imo*/Fe-b, see Table 1, corresponds to the adsorption of iron ion in the outer imogolite surface where the Fe^{3+} ions are monolinked to an oxygen of the O_6 layer, taking a similar place to the H_7 hydrogen position in the imogolite outer surface, Figure 2a-2d. The oxidation state 3+ of the iron in the Imo/Fe-b structures was kept constant by surrounding the ion by three water molecules and two OH^- molecules in octahedral configuration. In order to analyze the iron concentration effects on the electronic properties of the silicon and germanium imogolite-like structures, a sequence of 4 models with similar structural characteristics to the Imo/Fe, Imo/Fe-a and Imo/Fe-b were built varying the number of iron ions in the model from 1 to 4 ($0.05 \leq x \leq 0.1$; $x = \text{Fe}/(\text{Fe} + \text{Al})$) for each case. Table 1 and the Supporting Information display the notation of the 12 model structural variations considered in this work where Al/Fe ratio was kept above the experimental fibrous morphology and non-iron-aggregation threshold of 9 (Al/Fe = 9; $x = 0.1$) reported by McBride et al.¹⁷

The iron containing imogolite models were structural optimized carrying out geometry optimizations of the radial nanotube dimension keeping the cell lengths a , b , and c constant during the geometry optimization. The non-dependence of the c length with respect to the iron content arises because the iron concentration in the cell is small with respect to the entire structure content; however, this restriction should be considered just as a first approach. The ab initio optimizations were carried out using unrestricted all electron DFT calculations as is implemented in the DMol³ code²⁹ with Double Numerical basis set (DN),³⁰ together with the Perdew–Wang exchange correlation functional, GGA-PW91.³¹ The geometries were optimized until the maximum force and displacement on the system were 0.004 Ha/Å and 0.005 Å, respectively, to ensure a near ground-state configuration. Because of the high level computational cost of the unrestricted calculations, all the ab initio calculations were performed considering only the Γ point in the reciprocal space, which provides a good qualitative description of the problem as it is shown and validated in previous work.²⁴

Electronic Structure Analysis

The electronic effects of the addition of iron ions into the imogolite systems are mainly displayed in the bandgap region giving rise to electronic contamination states. Figure 3a–d shows the electronic density of states (DOS), varying the iron content $x = \text{Fe}/(\text{Fe} + \text{Al})$, of the Si-*Imo*-Fe (isomorphic Al^{3+} substituted by Fe^{3+}) models compared with the DOS of the non iron content imogolite-like system. In the curves of Figure 3a–d the DOS was split such that energy of the maximum of the valence bands of both systems coincides. The contamination of the bandgap by the Fe produces electronic states localized mainly in three bandgap regions: (a) in the top of the valence band, (b) in the bottom of the conduction band, and (c) in the middle of the bandgap, see insets in Figure 3a–d.

In the case of the silicon containing imogolite-like structures ($\text{M} = \text{Si}$ in Table 1), the small concentration of iron in the models does not alter significantly the shape of

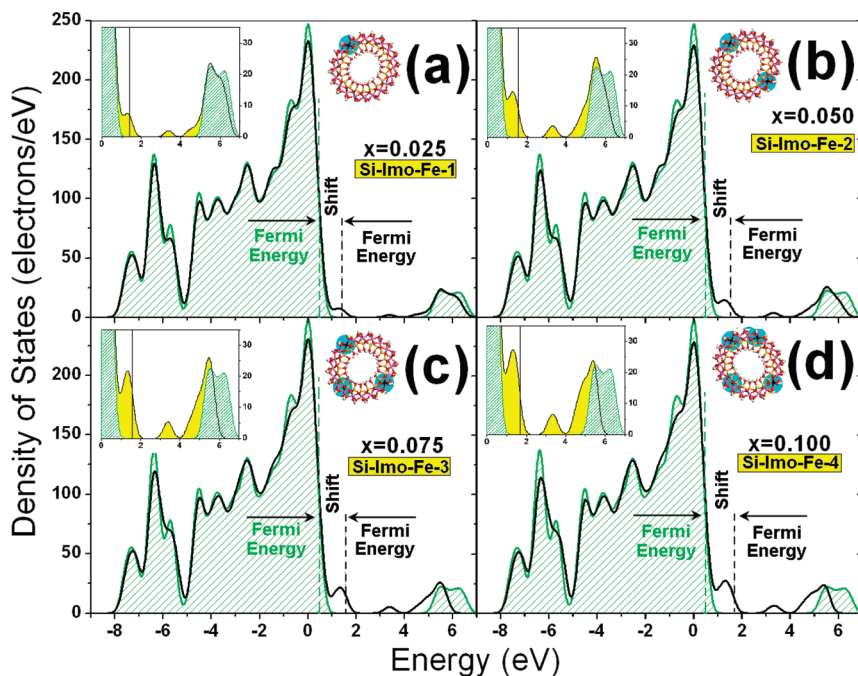


Figure 3. (a–d) Total DOS of the Fe isomorphic substituted imogolite structures: Si-Imo-Fe. The DOS of the iron containing models were compared with DOS of the non-containing models, green dashed line. The insets in a–d show the bandgap region where the new defect states were yellow highlighted. Finally, the dashed line indicates the Fermi energy for the both Fe containing and non containing imogolite-like models.

the valence band outside the bandgap region; however, the defects generated by the iron on the imogolite-like structures produce a shift of the largest occupied state, Fermi energy, with respect to the uncontaminated case, indicated as a dashed line in Figure 3a–d. The Fermi energy shift and the energy localization of defect states in the bandgap region are almost independent of the of the iron content in the models, generating a reduction of the bandgap value from ~4.6 eV in the case of non-iron-containing model²⁴ to 1.49, 1.69, 1.67, and 1.97 eV for the isomorphic substituted Si-Imo-Fe-1, Si-Imo-Fe-2, Si-Imo-Fe-3, and Si-Imo-Fe-4 models, respectively. In the case of the sequence of silicon imogolite-like models denoted as (Si/Imo-Fe-a and Si/Imo-Fe-b), the localization of the defect electronic states in the DOS displays similar characteristics and bandgap values to those analyzed in the Si-Imo-Fe models, see Figures S3–S4 in the Supporting Information.

On the other hand, the presence of germanium on the imogolite-like models, M = Ge in Table 1, seems not to affect drastically the behavior of the electronic states observed for the case of silicon imogolite models. Figure 4a–d displays the DOS for the Ge/Imo-Fe-b models where, like in the case of Si-Imo-Fe models, the DOS curves of the non-iron-containing and iron-containing Ge/Imo-Fe-b models were split in such away that the energy of the maximum of the valence bands of both systems coincide. The insets of Figure 4a–d show the difference in the curves between the non-iron-containing and iron-containing Ge/Imo-Fe-b models in the bandgap region observing a shift of the Fermi energy together with the presence of defect states in the top, middle, and bottom of the bandgap region like in the case of the silicon imogolite-like models. The bandgap values on germanium containing imogolite-like structures, the DOS,

display a larger iron dependence than in the silicon case having values of 2.6, 1.00, 0.94, and 0.9 eV for the Ge/Imo-Fe-b-1, Ge/Imo-Fe-b-2, Ge/Imo-Fe-b-3, and Ge/Imo-Fe-b-4 models, respectively. Similar iron concentration bandgap dependence is observed for the systems Ge-Imo-Fe and Ge-Imo/Fe, see Figures (S5–S6) in the Supporting Information.

With the aim of discerning the origin of the defect states in the DOS curves, an analysis of the correlation between the electronic states within the DOS and the geometric radial position in the nanotube structure through the local density of states (LDOS) was carried out in the Si/Imo-Fe-b-4 and Ge/Imo-Fe-a-4 models whose results are displayed in Figures 5 and 6. The top of the valence band, in both Si/Imo-Fe-b-4 and Ge/Imo-Fe-a-4 models, has the main contributions from the oxygen layers of the imogolite-like structure (O₂, O₄, O₆). These oxygen weights are similar to previous works in non-iron-containing aluminosilicate and aluminogermanate nanotube models.²⁴ However, in iron content cases there are an additional contribution coming from the hydration sphere of the iron ion states, see Figures 5a–c, 6a–c, and S7–S12 in the Supporting Information. On the other hand, the main contributions to the valence band shoulder generated by the shift of the Fermi energy come from states linked to the iron, hydration, and O₆ atoms in the case of the Si/Imo-Fe-b-4 model, whereas in almost all the analyzed cases the main contributions to the shoulder of the top valence band are connected to the iron ion and to the O₄ imogolite-like layer, Figures 5, 6, and S7–S12 in the Supporting Information.

In all the cases, the middle bandgap electronic states are almost exclusively associated to the iron ions, whose importance grows when the iron content is increased. An example of these contributions is the composition of the DOS peak at the top of the conduction bandgap region which has

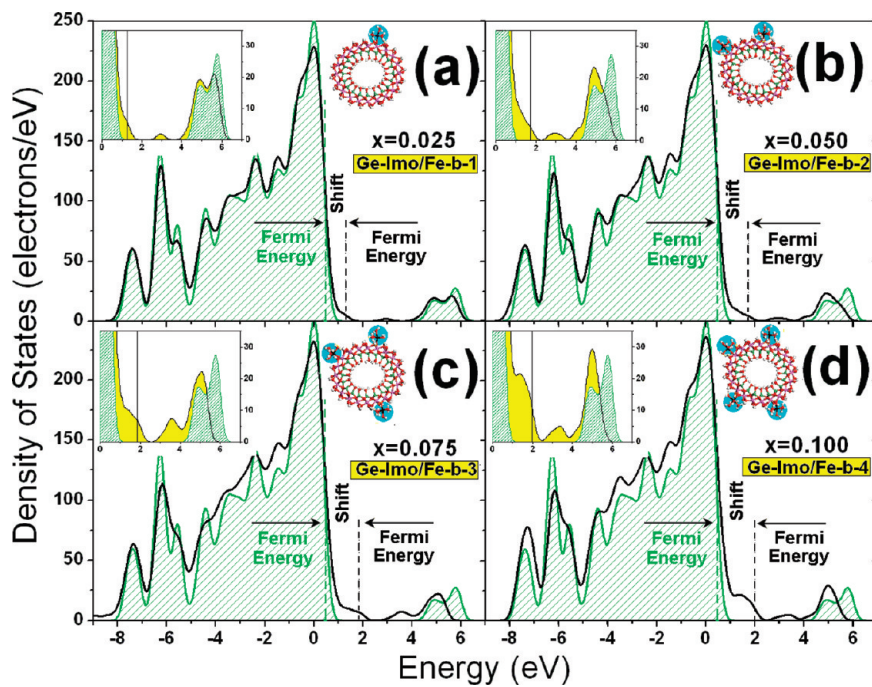


Figure 4. (a–d) Total DOS of the Fe ion adsorbed on the outer imogolite-like surface models: Ge-Imo/Fe-b. The DOS of the iron-containing models were compared with DOS of the non-iron-containin models, green dashed line. The insets in a–d shows the bandgap region where the new defect states were yellow highlighted. Finally, the dashed line indicates the Fermi energy for the both Fe containing and non containing imogolite-like models.

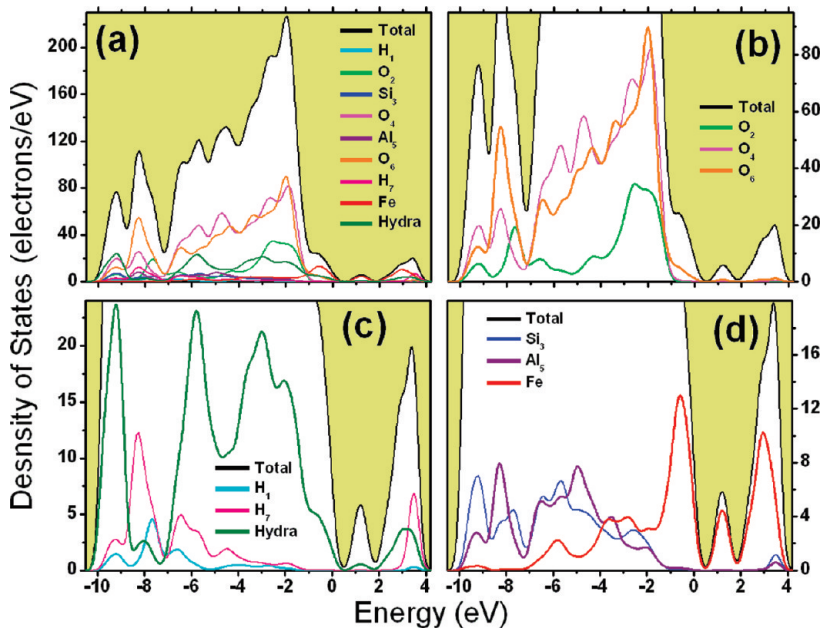


Figure 5. (a) Overview of the local density of states contribution to the total DOS for the Si-Imo/Fe-b-4, the notation indicates the atomic layer whereas hydra is the notation for the hydration sphere of Fe. (b) Zoom of the oxygen contribution to DOS. (c) Zoom to the hydrogen and hydration contribution to DOS. (d) Zoom of the Si_3 , Al_5 , and Fe to the DOS.

a high contribution of Fe states with smaller contributions coming from the hydration iron sphere. Additional contributions to this peak come from the H_7 and O_6 in the case of Si/Imo-Fe-b-4 model, whereas for the Ge/Imo-Fe-a-4 model the H_7 , O_6 and Ge_3 atomic layers also contribute to this peak. Similar aspects in the DOS partial contributions are shown by the rest structures, Figures S5–S12 in the Supporting Information. Because of the previous analysis, it is concluded that the inclusion of iron in the imogolite-

like structure adds new electronic states to the DOS associated to the Fe ion and their hydration sphere which are overlapped and shifted from the original imogolite states.

The distribution of the electronic states around the Fermi energy displayed in Figures 5, 6, and S7–12 in the Supporting Information clearly shows a high localization around the ion atoms. This localization phenomenon is also present when the spin density of states (spin-DOS) are analyzed, Figures 7 and S13–18 in the Supporting Information. In particular, Figure

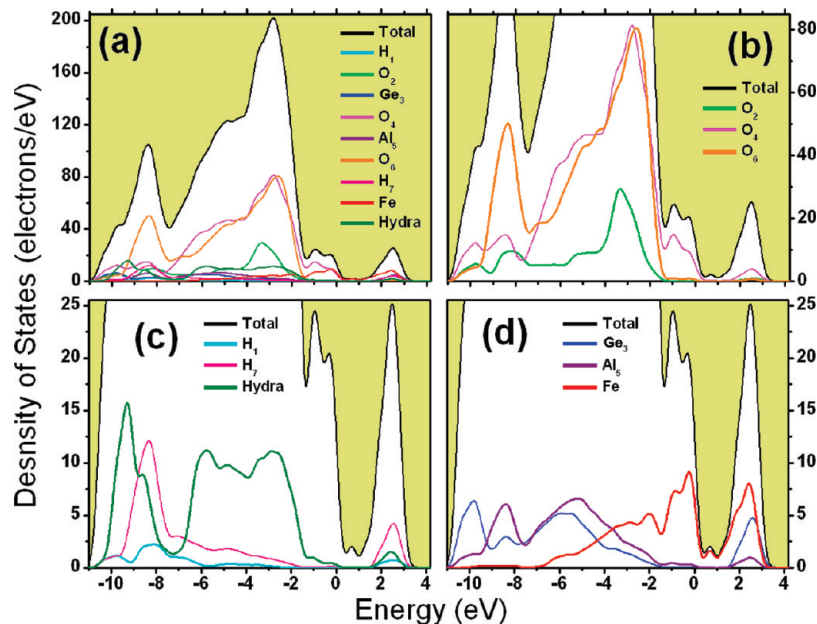


Figure 6. (a) Overview of the local density of states contribution to the total DOS for the Ge-Imo/Fe-a-4, the notation indicates the atomic layer whereas hydra is the notation for the hydration sphere of Fe. (b) Zoom of the oxygen contribution to DOS. (c) Zoom to the hydrogen and hydration contribution to DOS. (d) Zoom of the Ge_3 , Al_5 and Fe to the DOS.

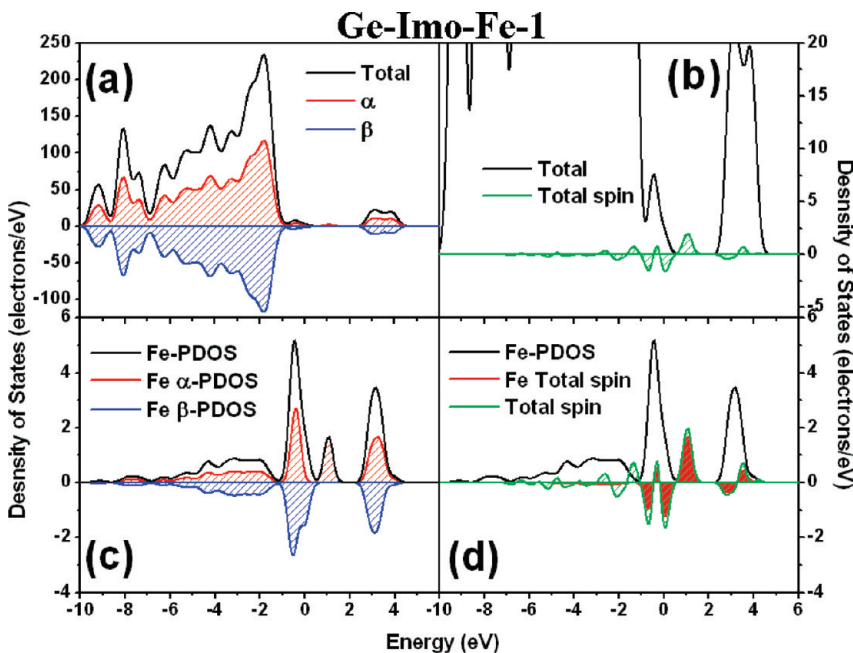


Figure 7. Spin-DOS of the system Ge-Imo-Fe-1. (a) α and β spin DOS contribution to Total DOS (b) Relative position and weight of the total spin DOS with respect to the Total DOS respect to the Total DOS. (c) Fe PDOS and its relative α and β spin PDOS. (d) Relative positions and weights of the Fe-PDOS, Fe Total spin, and the total spin of the model.

7a depicts the spin-DOS for the case Ge-Imo-Fe1 where the α and β spin-DOS shows similar shape and weights outside the band gap region. The spin difference between the α and β DOS displays, clearly, the localization of the total spin densities around the bandgap region, showing additionally an oscillatory behavior of the total spin-DOS in this region, Figure 7b. A closer analysis of the nature of the spin-DOS displays that the main contribution to the spin-DOS in the bandgap region is linked to iron ions incorporated in the structures being this phenomena common to all the analyzed structures, as is depicted in Figures 7c-d and S13-S18 in the Supporting Information.

As regards the final spin of the configurations, the imogolite-like structures displays in most cases a doublet configuration (spin = 1/2), when the number of iron ions is even, and singlet spin configuration (spin = 0) when number of iron ions is odd. The exceptions to this behavior are the following cases: Si-Imo/Fe-a-2, Si-Imo-Fe-4, Si-Imo/Fe-b-4, Ge-Imo-Fe-2, Si-Imo/Fe-b-4, and Si-Imo/Fe-b-4 with triplet spin configuration ($s = 1$).

The localization of the Fermi energy orbitals around the iron atoms is ratified by the geometric distribution of the HOMO and LUMO orbitals. In particular, Figure 8 shows

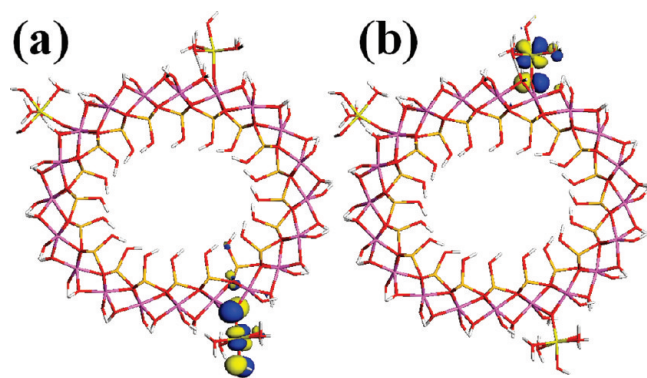


Figure 8. (a) Iso-surface with value 0.01 of the HOMO orbital for the structure Si-Imo/Fe-b-3. (b) Iso-surface with value 0.01 of the LUMO orbital for the structure Si/Imo-Fe-b-3. Clearly the both orbitals are localized around the Fe ion.

the spatial distribution of the isosurface with a value 0.01 for the Si/Imo-Fe-b-3 model where the localization of the HOMO and LUMO orbitals, around the position of two of the Fe atoms, is displayed. Note that the HOMO orbital is localized only in one of the three Fe atoms whereas the LUMO orbital is localized in a different Fe atom. The localized orbital linked to the third Fe ion is energetically situated in the neighborhood of the Fermi energy.

Reach and Limitations of the Bandgap Calculation

With the aim test the reach and limitations of the GGA-PW91 the band gap values in the case of Fe-aluminosilicate and Fe-aluminogermanate systems with respect to other DFT-functional

approaches, a sequence of calculations were carried out using 3 types of functionals: GGA-PW91,³¹ the revised Perdew–Burke–Ernzerhof GGA-RPBE,³² and the hybrid B3LYP.^{33,34} As test system, we have chosen a set of iron-containing flat imogolite-like structures with cell dimensions $a = 8.46 \text{ \AA}$, $b = 9.8 \text{ \AA}$, which corresponds to two gibbsite-like units. To ensure an empty atom gap between the imogolite-like layers the c length was selected as 20 Å. The iron ions were placed in configurations similar to those used on the tubular configuration, subst, inner/abs, and outer/abs, as is depicted in Figures 9 and S19–S23 in the Supporting Information. Like in the case of tubular structures, the electronic DOS calculations were carried out using the Γ point approximation and spin-unrestricted methodology. For both GGA-PW91 and GGA-RPBE, the calculations were carried out using the orbital localized code DMol³ with all electron approach where the iron imogolite-like surface was geometry optimized using the GGA-PW91 and the GGA-RPBE functionals respectively. On the other hand the hybrid-B3LYP the DOS calculations were carried out using the pseudopotential plane wave CASTEP code,³⁵ where the iron ion-imogolite-like system was geometry optimized using the GGA-PW91.

The results of the DOS calculations in flat iron-containing models show, in general, similar DOS shape and bandgap values independently of the DFT approach. In the case of the hybrid-B3LYP functional the middle bandgap states have a lower height with respect to the DOS than the GGA-PW91 and GGA-RPBE functionals; however, the middle bandgap states that define the bandgap value are still present in the hybrid-B3LYP DOS calculations with gap values comparable to those found in the flat and tubular imogolite-like structures.

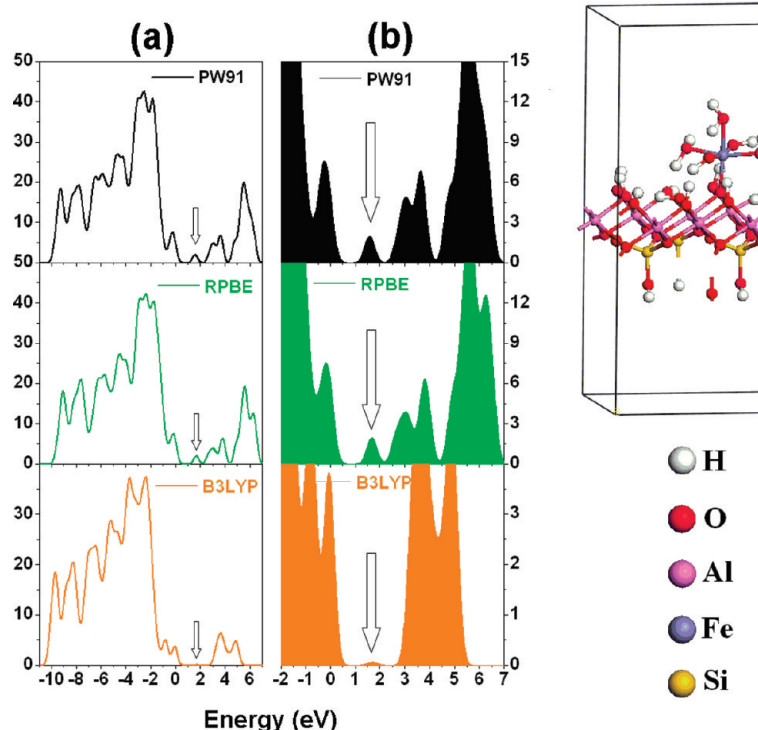


Figure 9. (a) DOS of silicon containing flat imogolite structure using the functionals PW91, RPBE, and B3LYP. This system is similar to the configurations outer/abs: $H_{87}O_{145}Al_{40}Fe_1Si_{20}$, $H_{94}O_{150}Al_{40}Fe_2Si_{20}$, $H_{101}O_{155}Al_{40}Fe_3Si_{20}$, and $H_{108}O_{160}Al_{40}Fe_4Si_{20}$ of the Table 1. (b) Zoom of the DOS depicted where is displayed the middle bandgap states.

This phenomenon is most clearly displayed by the subst. and outer/abs configurations, Figures 9 and S19–S21 in the Supporting Information. On the other hand the flat inner/abs configurations shows larger discrepancies between the GGA-PW91 and GGA-RPBE and the hybrid B3LYP calculations in the bandgap region due to the larger water versus Si–OH and Ge–OH interaction in this configurations, Figures S22–S23 in the Supporting Information. On the basis of these calculations, some qualitative and quantitative aspects of the DOS of iron containing imogolite-like systems and the order or magnitude of the bandgap found in the tubular imogolite-like structures are validated, at least in terms of the DFT.

Conclusions

The electronic properties of isomorphic substituted and adsorbed iron aluminosilicate and aluminogermanate nanotube structures were analyzed based on all electrons unrestricted ab initio calculations. The optimized nanotube models have iron content in the interval $0.05 \leq x \leq 0.1$ and varying iron ion positions in three different octahedral configurations: inner, outer imogolite surface and isomorphic substituted in the Al gibbsite layer. In all the configurations and content cases the electronic Fe-imogolite-like silicate/gemanate DOS displays large changes because of the contamination by Fe electronic states of the bandgap region, generating the reduction of the gap values from ~ 4.7 to $[2.0\text{--}1.4\text{ eV}]$ and from ~ 4.2 to $[2.6\text{--}1.0\text{ eV}]$ for the Fe-silicon and Fe-germanium imogolite-like nanotubes. The Fe inclusion into the imogolite-like structures produces a shift of the Fermi energy and the overlapping of Fe electronic states to the original imogolite-like states at the top, the middle, and the bottom of the gap region.

Supporting Information Available: Figures showing snapshots of optimized iron-containing aluminosilicates and aluminogermanate, DOS of the imogolite–iron dimer, adsorbed Fe–imogolite over the inner imogolite surface, isomorphic substituted Al by Fe in germanium-containing nanotube, adsorbed imogolite over the inner imogolite surface, germanium-containing flat imogolite structure, and silicon-containing flat imogolite structure, sequence of total DOS and PDOS, and sequence of spin-DOS. This material is available free of charge via the Internet at <http://pubs.acs.org>.

References

- (1) Yoshinaga, N.; Aomine, S. *Soil Sci. Plant Nutr. (Tokyo)* **1962**, *8*, 22–29.
- (2) Wada, K.; Yoshinaga, N. *Am. Mineral.* **1969**, *54*, 50–71.
- (3) Wada, S.-I.; Eto, A.; Wada, K. *J. J. Soil Sci.* **1979**, *30*, 347–355.
- (4) Wada K. In *Minerals in Soil Environments*, 2nd ed.; Soil Science Society of America: Madison, WI, 1989.
- (5) Farmer, V. C.; Fraser, A. R.; Tait, J. M. *J. Chem. Soc., Chem. Commun.* **1977**, *13*, 462–463.
- (6) Mukherjee, S.; Kim, K.; Nair, S. *J. Am. Chem. Soc.* **2007**, *129*, 6820–6826.
- (7) Levard, C.; Rose, J.; Masion, A.; Doelsch, E.; Borschneck, D.; Olivi, L.; Dominici, C.; Grauby, O.; Woicik, J. C.; Bottero, J.-Y. *J. Am. Chem. Soc.* **2008**, *130*, 5862–5863.
- (8) Yang, H.; Wang, C.; Su, Z. *Chem. Mater.* **2008**, *20*, 4484–4486.
- (9) Denaix, L.; Lamy, I.; Bottero, J. Y. *Colloids Surf., A* **1999**, *158*, 315–325.
- (10) Ackerman, W. C.; Smith, D. M.; Huling, J. C.; Kim, Y.-W.; Bailey, J. K.; Brinker, C. J. *Langmuir* **1993**, *9*, 1051–1057.
- (11) Masaya, S.; Shin, S.; Masaki, M.; Shinji, T.; Tadato, M. *J. Ceram. Soc. Jpn.* **2001**, *109*, 874–881.
- (12) Imamura, S.; Kokubu, T.; Yamashita, T.; Okamoto, Y.; Kajiwara, K.; Kanai, H. *J. Catal.* **1996**, *160*, 137–139.
- (13) Ookawa, M.; Inoue, Y.; Watanabe, M.; Suzuki, M.; Yamaguchi, T *Clay Sci.* **2006**, *12*, 280–284.
- (14) Nordstrand R. A., U.S. Patent 4394253, 1984.
- (15) Hirohisa, Y.; Michalik, J.; Sadlo, J.; Perlinska, J.; Takenouchi, S.; Shimomura, S.; Uchida, Y. *Appl. Clay Sci.* **2001**, *19*, 173–178.
- (16) Nakagaki, S.; Wypych, F. *J. Colloid Interface Sci.* **2007**, *315*, 142–157.
- (17) MacBride, M. B.; Farmer, V. C.; Russell, J. D.; Tait, J. M.; Goodman, B. A. *Clay Miner.* **1984**, *19*, 1–8.
- (18) Ugolini, F. C.; Dahlgren, R. A. *Soil Sci. Soc. Am. J.* **1991**, *55*, 1166–1171.
- (19) Taylor, R. M.; Raupach, M.; Chartres, C. J. *Clay Miner.* **1990**, *25*, 375–389.
- (20) Imamura, S.; Hayashi, Y.; Kajiwara, K.; Hoshino, H.; Kaito, C. *Ind. Eng. Chem. Res.* **1993**, *32*, 600–603.
- (21) Lee, Y.; Kim, B.; Yi, W.; Takahara, A.; Sohn, D. *Bull. Korean Chem. Soc.* **2006**, *27*, 1815–1818.
- (22) Wada, S.; Wada, K. *Clays Clay Miner.* **1982**, *30*, 123–128.
- (23) Cradwick, C. P. G.; Farmer, V. C.; Russell, J. D.; Masson, C. R.; Wada, K.; Yoshinaga, N. *Nat. Phys. Sci.* **1972**, *240*, 187–189.
- (24) Alvarez-Ramírez, F. *Phys. Rev. B* **2007**, *76*, 125421–1–125421–14.
- (25) Li, H.; Mahanti, S. D.; Pinnavaia, T. J. *J. Phys. Chem. B* **2005**, *109*, 2679–2685.
- (26) Gale, J. D.; Rohl, A. L.; Milman, V.; Warren, M. C. *J. Phys. Chem. B* **2001**, *105*, 10236–10242.
- (27) Refson, K.; Park, S.-H.; Sposito, G. *J. Phys. Chem. B* **2003**, *107*, 13376–13383.
- (28) Teobaldi, G.; Beglitis, N. S.; Fisher, A. J.; Zerbetto, F.; Hofer, W. A. *J. Phys.: Condens. Matter* **2009**, *21*, 95301–95309.
- (29) S. D. I. DMol3. User Guide, release 4.0.
- (30) Delley, B. *J. J. Chem. Phys.* **2000**, *113*, 7756–7764.
- (31) Perdew, J. P.; Wang, Y. *Phys. Rev. B* **1992**, *45*, 13244–13249.
- (32) Hammer, B.; Hansen, L. B.; Nørskov, J. K. *Phys. Rev. B* **1999**, *59*, 7413–7421.
- (33) Kim, K.; Jordan, K. D. *J. Phys. Chem.* **1994**, *98*, 10089–10094.
- (34) Stephens, P. J.; Devlin, F. J.; Chabalowski, C. F.; Frisch, M. J. *J. Phys. Chem.* **1994**, *98*, 11623–11627.
- (35) Clark, S. J.; Segall, M. D.; Pickard, C. J.; Hasnip, P. J.; Probert, M. J.; Refson, K.; Payne, M. C. Z. *Kristallogr.* **2005**, *220*, 567–570.